energy&fuels

pubs.acs.org/EF

Article

Shale Gas Production Evaluation Considering Gas Diffusion and Dispersed Distribution of Kerogen

Yifan Huang,* Jishan Liu, Qi Gao, Derek Elsworth, and Yee-Kwong Leong

Cite This: *Energy Fuels* 2024, 38, 1083−1097

Read Online

ACCESS | Metrics & More | Article Recommendations

Downloaded via PENNSYLVANIA STATE UNIV on May 16, 2024 at 17:01:14 (UTC).
See https://pubs.acs.org/sharingguidelines for options on how to legitimately share published articles.

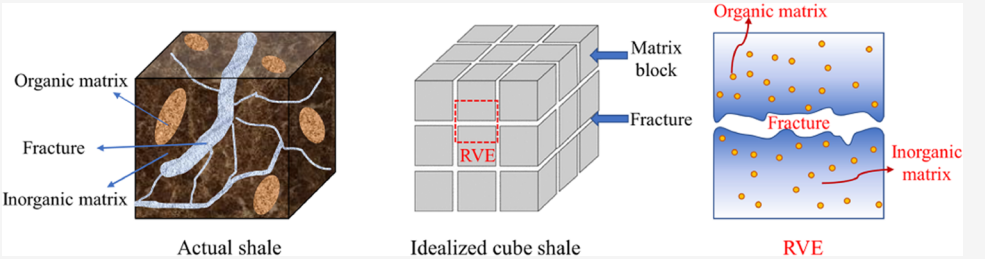

ABSTRACT: In the shale matrix, organic matter (kerogen) is dispersed and embedded within an inorganic matrix, and its internal gas diffusion is a long-term process. Under the influence of the transient process and complex structure, pressure and Langmuir's strain constant in the matrix are typically distributed nonuniformly. This implies that the sorption-induced swelling/shrinkage in the matrix would also present a nonuniform distribution, and the resulting matrix−fracture mechanical interactions have significant impacts on gas flow in shale fractures as well as gas production. In this study, through the concepts of the swelling path and swelling triangle, the nonuniform swelling/shrinkage is characterized, thereby establishing the relationship between shale response and swelling/shrinkage behaviors. In addition, given that gas transport in organic and inorganic matrixes is typically governed by different mechanisms, the influence of the compositional heterogeneity on gas flow in the matrix is also investigated. Subsequently, novel shale permeability and gas flow models are developed, incorporating the effects of gas diffusion and the dispersed distribution of kerogen. The proposed concepts and developed models are validated by comparing simulation results with one set of experimental observations, as well as two sets of field production data. Our results suggest that neglecting the mechanisms induced by the transient process and complex structure would lead to inaccurate estimations of shale permeability during gas production and result in underestimations of both gas production rates and cumulative production.

1. INTRODUCTION

Shale gas has emerged as one of the most essential energy supplies in the world due to its abundant reserves, widespread distribution, and lower carbon emissions compared to other fossil fuels (such as coal and oil).[1−4] Permeability, as a crucial property that determines gas flow characteristics within reservoirs, plays a significant role in shale gas production. It is affected by multiple factors that involve the coupling of fluid flow and solid deformation, including effective stress changes, gas adsorption/desorption, and flow regime effects, and exhibits a dynamic evolutionary trend during shale gas production.[5−11] In order to have a thorough comprehension of the shale permeability evolution and thus pave the way toward shale gas development, great efforts have been made. Experimental measurements undeniably offer the most direct means of observing permeability and associated gas flow characteristics, but they typically come at the expense of time-consuming and labor intensiveness, coupled with the limitations in the results obtained.[12,13] An alternative way is to explore how shale responds to gas extraction by developing theoretical models. Currently, continuum models (such as dual porosity/permeability models) are widely used because of their benefits of cost-effective computation and low input data requirements.[14]

Typically, shale is idealized as a dual porosity medium (i.e., matrix and natural fractures) to capture the nature of hierarchical pore structures.[15,16] Following depressurization, gas in natural fractures flows to wellbores or hydraulic fractures, while gas in the matrix diffuses into adjacent natural fractures before being produced. In general, permeability for fractures is several orders of magnitude larger than that for matrix. As a result, gas is able to flow rapidly in fractures, while gas diffusion in the matrix exhibits a slow pace, lasting from

Received: October 1, 2023
Revised: December 18, 2023
Accepted: December 19, 2023
Published: December 29, 2023

ACS Publications

© 2023 American Chemical Society

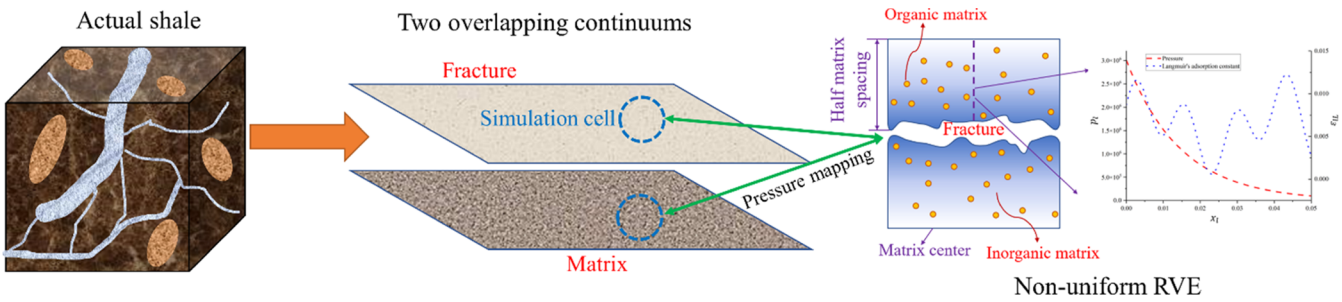

Figure 1. Dual porosity/permeability model based on nonuniform RVE.

days to months.[17−19] This means that during gas production, shale is mainly in nonequilibrium states.[6,8,20,21] During nonequilibrium periods, matrix pressure exhibits a nonuniform distribution from the fracture wall to the inner matrix.[17,20,22] In addition, under the influence of environmental conditions, geological history, and chemical reactions during formation, the shale matrix comprises multiple minerals, which can broadly be classified into organic matter (kerogen inclusions) and inorganic matrix (including clay, quartz, and pyrite).[23−26] The scanning electron microscopy (SEM) and transmission electron microscopy (TEM) results reveal that organic matter is dispersedly embedded within an inorganic matrix.[27−29] These two matrix components present significant differences in physical properties, particularly in their sorption capacities.[12,26,30] In this case, Langmuir's strain constant in the shale matrix exhibits a high degree of heterogeneity.

According to the Langmuir adsorption isotherm, the adsorption-induced swelling or desorption-induced shrinkage is a function of pressure and Langmuir's strain constant, which can be defined by a Langmuir-type equation.[31] Therefore, under the effect of long-term gas diffusion and the staggered distribution of the two matrix components, the matrix swelling/shrinkage should present a nonuniform distribution. This swelling/shrinkage behavior has been documented in the laboratory by mounting a distributed array of strain gauges on the sample surface to measure the real-time strain evolution during gas injection.[20] The nonuniform swelling/shrinkage has long been identified as the root cause for why the adsorption-induced swelling or desorption-induced shrinkage is involved in the permeability evolution, even under stress-controlled boundary conditions.[32,33] Specifically, when the matrix swells or shrinks nonuniformly, matrix deformation would not only contribute to the shale bulk but also affect natural fractures, inducing matrix−fracture mechanical interactions.[17,34] Under the effect of the mechanical interactions, the natural fracture aperture and its associated permeability change, thereby influencing the gas flow characteristics therein. In addition, gas flow in the inorganic and organic matrices is generally influenced by different mechanisms, and the total gas flux in the matrix should be the sum of the gas flux in the organic and inorganic parts.[35−39] This implies that there is a close relationship between gas flow characteristics within the matrix and the compositional heterogeneity.[40,41] Therefore, when investigating shale matrix permeability, it is imperative to take into account respective flow mechanisms within each component as well as the proportion of these two matrix components.

Although long-term gas diffusion and the dispersed distribution of organic matter in the inorganic matrix would result in mechanisms that affect permeability and gas flow characteristics in shale, in existing continuum models, these important mechanisms have not been fully taken into account. Under the continuum framework, the representative volume element (RVE) is the foundation for analysis, from which governing equations are established, and then macroscopic phenomenological constitutive relationships are derived.[18,42−45] In existing models, the underlying RVE is treated as a mathematical construct (called the simulation cell).[13,34] This treatment results in the loss of spatial information within the RVE. Each physical property (such as Langmuir's strain constant) and state variable (such as pressure) for matrix and fractures in the RVE are represented by only one value.[33,46−48] In this case, the distribution of state variables and physical properties within the RVE can only be regarded as uniform, which implies that its internal occurring transient processes and complex structures are ignored. Consequently, models derived based on the uniform RVE do not incorporate the mechanisms induced by these two factors. These models struggle to adequately explain current experimental observations, thereby hindering their ability to yield satisfactory results in predicting gas shale production as well.[12,49−52] For example, these models suggest that shale permeability is related only to the effective stress and is independent of the gas sorption effect. Nevertheless, these conclusions are not consistent with experimental observations reported in the literature.[49] We hypothesize that the neglect of gas diffusion and the dispersed distribution of organic matter, along with the mechanisms induced by both, is the fundamental reason for the deficiencies in existing models. The primary objective of this study is to resolve this knowledge gap.

2. MODEL DEVELOPMENT

In dual porosity/permeability models, the macroscale geometry of shale is presented by two overlapping continuums, while the microscale structure is characterized by the RVE with matrices and fractures.[53] In order to incorporate gas diffusion and the dispersed phase of kerogen into the underlying RVE, we discard the traditional uniform RVE and instead introduce a novel nonuniform RVE where the distribution of pressure and Langmuir's strain constant is nonuniform. Moreover, through a pressure mapping method, the nonuniform RVE is embedded into a macroscale continuum, as shown in Figure 1. Subsequently, shale permeability and gas flow models that incorporate the mechanisms induced by the transient process and complex structure are developed.

2.1. Characterizing Gas Diffusion and Dispersed Distribution of Organic Matter within RVE. As a porous medium with complex structures and multiple components, analyzing gas diffusion in the matrix and evaluating the pressure distribution during this process is challenging but can

https://doi.org/10.1021/acs.energyfuels.3c03774
Energy Fuels 2024, 38, 1083−1097

be dealt with by some simplifications and assumptions. In this study, gas diffusion within a matrix is conceptualized as one-dimensional pressure diffusion within a cubic region, with the fracture wall as the base and a half-matrix spacing as the height.[13,54,55] In this case, the boundary conditions can be treated as follows: pressure at the fracture wall is considered to align with fracture pressure, while at the matrix center (located half-matrix spacing away from the fracture wall), due to symmetry, the mass flux is regarded to be zero here. Moreover, in order to obtain an explicit closed-form solution for the one-dimensional diffusion equation to calculate the pressure distribution during gas diffusion, some assumptions need to be introduced to linearize the diffusion equation,[56] including (a) gas contained within matrix is ideal; (b) gas viscosity, porosity, and permeability are uniform and remain unchanged; and (c) the impact of gas sorption is negligible. Under this condition, the pressure distribution can be derived

$$p_{\mathrm{lm}}(x_{\mathrm{l}}, t_{\mathrm{l}}) = \sum_{n=0}^{\infty} \frac{4(p_{\mathrm{i}} - p_{\mathrm{lf}})}{(2n+1)\pi} e^{-\left[\left(\frac{(2n+1)\pi}{2L}\right)^2 \frac{k_{\mathrm{m_{app_0}}}}{\varphi_{\mathrm{m_0}} \mu c_t}\right] t_{\mathrm{l}}} \sin\frac{(2n+1)\pi x_{\mathrm{l}}}{2L} + p_{\mathrm{lf}} \tag{1}$$

where p_{lm} and p_{lf} are the pressure in matrices and fractures within the nonuniform RVE, respectively; $\varphi_{\mathrm{m_0}}$ and $k_{\mathrm{m_{app0}}}$ are the initial matrix porosity and apparent permeability; μ is the gas viscosity; c_t is the gas compressibility; p_{i} is the initial pressure; t_{l} is the characteristic time; x_{l} is the space variable; and L refers to the half-length of the matrix spacing.

A notable distinction between the organic and inorganic matrices is their different sorption capacities. Therefore, to implement the characterization of the dispersed distribution of organic matter in the inorganic matrix within the RVE, we first randomly generate Langmuir's strain constant and subsequently introduce a threshold to differentiate these two components, as shown in Figure 2. In this study, the threshold is defined as 0.005. This is because previous publications have demonstrated that the shale matrix possesses an average strain constant of 0.005, with its value primarily governed by inorganic matter.[15,21,57] In this case, an area is classified as part of the organic matrix if its strain constant is greater than or equal to 0.005 and as part of the inorganic matrix if it is less than 0.005

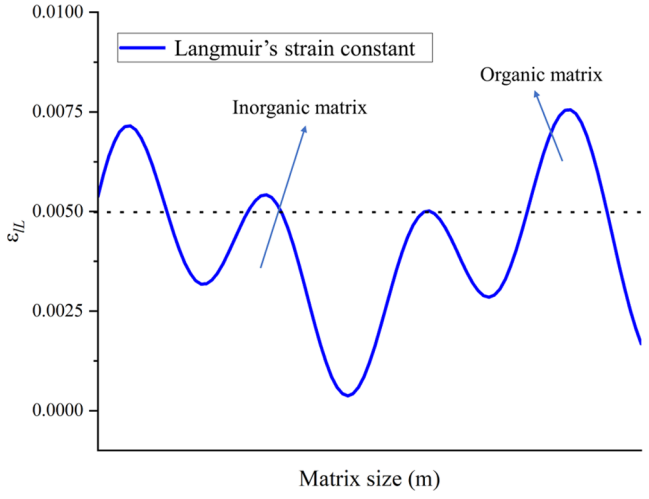

Figure 2. Illustration of the dispersed distribution of the organic matrix within the inorganic matrix.

$$j = \begin{cases} 1, & \text{if } \varepsilon_{\mathrm{lL}} \geq 0.005 \\ 2, & \text{if } \varepsilon_{\mathrm{lL}} < 0.005 \end{cases} \tag{2}$$

where $j = 1$ refers to the organic matrix and $j = 2$ refers to the inorganic matrix; $\varepsilon_{\mathrm{lL}}$ is the Langmuir's strain constant in the nonuniform RVE. The random Langmuir's strain constant is assumed to follow a Weibull statistical distribution,[58,59] which can be expressed as

$$\mathrm{f}(\varepsilon_{\mathrm{lL}}) = \frac{\tau}{\lambda}\left(\frac{\varepsilon_{\mathrm{lL}}}{\lambda}\right)^{\tau-1} e^{-\left(\frac{\varepsilon_{\mathrm{lL}}}{\lambda}\right)^{\tau}} \tag{3}$$

where λ is the scale parameter and τ is the shape parameter. Based on the Langmuir adsorption isotherm, the nonuniform distribution of the matrix swelling/shrinkage caused by the transient process and complex structure can be obtained

$$\varepsilon_{\mathrm{ls}}(x_{\mathrm{l}}, t_{\mathrm{l}}) = \frac{\varepsilon_{\mathrm{lL}}(x_{\mathrm{l}}) p_{\mathrm{lm}}(x_{\mathrm{l}}, t_{\mathrm{l}})}{p_{\mathrm{lm}}(x_{\mathrm{l}}, t_{\mathrm{l}}) + p_{\mathrm{L}}} \tag{4}$$

where p_{L} is the Langmuir's pressure constant.

Under the continuum framework, the RVE would be treated as a simulation cell of macro-scale continuum representations, which has no volume, no area, and no length. To embed the established nonuniform RVE with spatial information into continuum representations and utilize it as the basis for constructing overall permeability and gas flow models, a pressure mapping method is employed.[13] In this method, at each simulation cell, there is a local nonuniform RVE corresponding to it, and the pressure results at the simulation cell are treated as average pressure in the local RVE. This means that matrix pressure (p_{gm}) and fracture pressure (p_{gf}) at the simulation cell calculated by overall formulations are equal to average matrix pressure ($\overline{p_{\mathrm{lm}}}$) and fracture pressure (p_{lf}) in the nonuniform RVE, respectively. Based on the diffusion equation, the average pressure of the matrix block within the nonuniform RVE can be derived as

$$\overline{p_{\mathrm{lm}}}(t_{\mathrm{l}}) = \sum_{n=0}^{\infty} \frac{8(p_{\mathrm{i}} - p_{\mathrm{lf}})}{[(2n+1)\pi]^2} e^{-\left[\left(\frac{(2n+1)\pi}{2L}\right)^2 \frac{k_{\mathrm{m_{app_0}}}}{\varphi_{\mathrm{m_0}} \mu c_t}\right] t_{\mathrm{l}}} + p_{\mathrm{lf}} \tag{5}$$

It can be seen that, after inputting p_{gf} and p_{gm} into eq 5, that is, replacing p_{gf} and p_{gm} with p_{lf} and $\overline{p_{\mathrm{lm}}}$, respectively, the characteristic time t_{l} can be calculated. After substituting the calculated t_{l} into eq 1, the pressure distribution in the local nonuniform RVE could be obtained. Through this pressure mapping method, the relationship between global continuum representations and the local nonuniform RVE is connected. It should be pointed out that after embedment, there would exist two systems, one of which is global representations (defined as the global system), and the other is the local embedded nonuniform RVE (defined as the local system). These two systems interact with each other. In order to avoid confusion, we employ the subscripts g and l to mark parameters as well as equations in the two systems, acting as the first element in the subscripts.

2.2. Swelling Path and Swelling Triangle. From eq 4, matrix swelling/shrinkage behaviors in the local system can be obtained. Under the combined effect of the transient process

https://doi.org/10.1021/acs.energyfuels.3c03774
Energy Fuels 2024, 38, 1083−1097

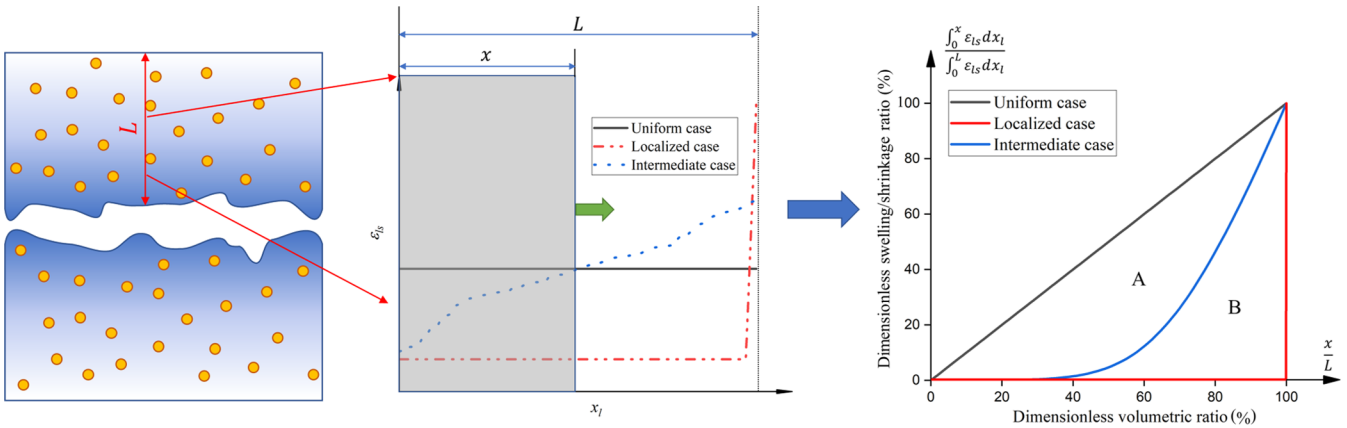

Figure 3. Schematic diagram of the swelling path and swelling triangle.

and complex structure, there are innumerable types of swelling/shrinkage behaviors with various distributions and magnitudes. It is difficult to determine shale response to each swelling/shrinkage behavior individually. The most feasible way is to quantify diverse swelling/shrinkage cases based on a measure. Consequently, the concept of the swelling path and swelling triangle is proposed.[33] In all behaviors, the case where the swelling/shrinkage is equal everywhere is defined as the uniform case, while the case where all swelling/shrinkage is localized at one region is defined as the localized case. In general, the actual distribution is somewhere between these two extreme cases, which is called the intermediate case. At first, the swelling/shrinkage for the three cases is rearranged from small to large. Subsequently, using the distance from the origin as a variable (x), the swelling/shrinkage is integrated with a variable upper limit ($\int_0^x \varepsilon_{ls} dx_l$). With the dimensionless volumetric ratio (x/L) as the X-axis and the dimensionless swelling/shrinkage ratio ($\int_0^x \varepsilon_{ls} dx_l / \int_0^L \varepsilon_{ls} dx_l$) as the Y-axis, swelling paths for the uniform, localized, and intermediate case would be generated, as shown in Figure 3.

It is evident that for the localized case, the dimensionless swelling/shrinkage ratio initially remains unchanged, but it experiences a nearly vertical ascent to reach 100 at the end (as shown by the red line). In contrast, for the other extreme case (the uniform swelling/shrinkage), the swelling path presents a linear upward trend with a slope of 1 as the dimensionless volumetric ratio increases (as shown by the black line). The swelling paths for the two cases delineate a triangle (called the swelling triangle), and the swelling paths for all intermediate cases lie within the triangle (as shown by the blue line). Any swelling path has the same start and end points, but different paths between these two ends reflect various swelling/shrinkage behaviors. Each swelling/shrinkage case has a unique swelling path corresponding to it. It is important to note that the concept we proposed is called the swelling path, yet it is possible to characterize both swelling and shrinkage behaviors. Based on the concept of the swelling path and triangle, a novel nonuniform swelling coefficient can be introduced to quantify the degree of the nonuniform swelling/shrinkage. For any given swelling path, we define the area between this swelling path and the diagonal line as A and that between this swelling path and perpendicular lines as B. After that, the nonuniform swelling coefficient is determined

$$\beta = \frac{B}{A + B} \tag{6}$$

It is evident that the position of the swelling path in the triangle would define the magnitude of the coefficient. Once the swelling path coincides with the boundaries of the triangle, $\beta = 1$ or $\beta = 0$. For intermediate cases, $0 < \beta < 1$.

2.3. Gas Flow in Natural Fractures. According to the mass conservation law and Darcy's law, the governing equation for gas flow and storage in shale natural fractures can be expressed[31]

$$\frac{\partial}{\partial t_g}\left(\varphi_{gf}\rho_{gf} + \rho_{ga}\rho_s \frac{V_{Lf} p_{gf}}{p_{gf} + p_L}\right) + \nabla\cdot\left(-\rho_{gf}\frac{k_{gf}}{\mu}\nabla p_{gf}\right) = -\frac{k_{gm_{app}}\rho_{gm}}{\mu}\psi(p_{gf} - p_{gm}) \tag{7}$$

where φ_{gf} is the fracture porosity; ρ_{gf} is the gas density in fractures; p_{gf} is the fracture pressure; ρ_{ga} is the gas density at standard conditions; ρ_s is the shale density; V_{Lf} is the Langmuir's volume constant for fractures; k_{gf} is the fracture permeability; $k_{gm_{app}}$ is the matrix apparent permeability; ρ_{gm} is the gas density in the matrix; and ψ is the mass transfer shape factor and is related to the matrix size (L) in the local embedded RVE, with dimensions of L^{-2}.

According to previous publications, there exists a typical cubic relation between permeability and porosity[22,60]

$$\frac{k_{gf}}{k_{gf_0}} = \left(\frac{\varphi_{gf}}{\varphi_{gf0}}\right)^3 \tag{8}$$

The change in porosity is related to the fracture and bulk volumetric increment[61,62]

$$\frac{\Delta\varphi_{gf}}{\varphi_{gf_0}} = \frac{\Delta V_{gf}}{V_{gf_0}} - \frac{\Delta V_{gb}}{V_{gb_0}} \tag{9}$$

where V_{gf} is the fracture volume and V_{gb} is the shale bulk volume. The subscript 0 refers to the initial value.

Shale bulk deformation is a function of the effective stress and the matrix swelling/shrinkage.[6] Therefore, volumetric changes in the shale bulk can be written as

$$\frac{\Delta V_{gb}}{V_{gb_0}} = -\left(\frac{\Delta\sigma_{con} - a\Delta p_{gf}}{K}\right) + \Delta\varepsilon_{gbm} \tag{10}$$

https://doi.org/10.1021/acs.energyfuels.3c03774
Energy Fuels 2024, 38, 1083−1097

where σ_{con} is the confining pressure (mean normal stress); K is the bulk modulus of shale; a is $1 - K/K_m$; K_m is the bulk modulus of the matrix; ε_{gbm} refers to the shale bulk strain induced by the matrix swelling/shrinkage.

Fracture deformation is a function of the effective stress, the sorption-induced fracture swelling/shrinkage, and the fracture strain induced by the matrix swelling/shrinkage (i.e., matrix−fracture mechanical interactions).[6,13] The volumetric change in fractures is

$$\frac{\Delta V_{gf}}{V_{gf_0}} = -\left(\frac{\Delta\sigma_{con} - a_f \Delta p_{gf}}{K_f}\right) + \Delta\varepsilon_{gfs} + \Delta\varepsilon_{gfm} \tag{11}$$

where K_f is the bulk modulus of fractures; a_f is $1 - K_f/K_m$; ε_{gfs} is the sorption-induced fracture swelling/shrinkage; ε_{gfm} is the fracture strain induced by the matrix swelling/shrinkage.

As mentioned in the Introduction, the fundamental reason for the matrix swelling/shrinkage not only affecting the shale bulk but also acting on fractures is the nonuniform swelling/shrinkage. In this study, we hypothesize that the proportion of the matrix swelling/shrinkage that contributes to bulk deformation is related to the degree of the nonuniform swelling/shrinkage. Specifically, when the distribution of the matrix swelling/shrinkage is uniform, all matrix swelling/shrinkage contributes to the shale bulk (aligning with conventional models based on the uniform RVE). Conversely, when the swelling/shrinkage is localized at one region, all matrix swelling/shrinkage acts on fractures. Therefore, according to the proposed nonuniform swelling coefficient and the volumetric relation between matrices and fractures ($V_{gf}/V_{gm} \approx \varphi_{gf0}/1$), changes in the bulk and fracture strain induced by the matrix swelling/shrinkage are derived as

$$\Delta\varepsilon_{gbm} = \beta\Delta\varepsilon_{gms} \tag{12}$$

$$\Delta\varepsilon_{gfm} = -\frac{(1-\beta)\Delta\varepsilon_{gms}}{\varphi_{gf0}} \tag{13}$$

The negative sign in eq 13 indicates that there is a negative correlation between the fracture strain and matrix swelling/shrinkage. The swelling/shrinkage for matrices and fractures is

$$\varepsilon_{gms} = \frac{\varepsilon_L p_{gm}}{p_L + p_{gm}} \tag{14}$$

$$\varepsilon_{gfs} = \frac{\varepsilon_L p_{gf}}{p_L + p_{gf}} \tag{15}$$

Substituting eqs 10−13 into 9 and then integrating it, we obtain the following relationship

$$\frac{\varphi_{gf}}{\varphi_{gf0}} = \exp\left(-\frac{1}{K_f}(\Delta\sigma_{con} - \Delta p_{gf}) + \Delta\varepsilon_{gfs} - \frac{(1-\beta)\Delta\varepsilon_{gms}}{\varphi_{gf0}} - \beta\Delta\varepsilon_{gms}\right) \tag{16}$$

After substituting eq 16 into eq 8, shale fracture permeability incorporating the influence of the nonuniform swelling/shrinkage can be derived as

$$\frac{k_{gf}}{k_{gf_0}} = \exp\left(3\left(-\frac{1}{K_f}(\Delta\sigma_{con} - \Delta p_{gf}) + \Delta\varepsilon_{gfs} - \frac{(1-\beta)\Delta\varepsilon_{gms}}{\varphi_{gf0}} - \beta\Delta\varepsilon_{gms}\right)\right) \tag{17}$$

Equation 17 reveals that shale fracture permeability is controlled by four items: effective stress changes, sorption-induced fracture swelling/shrinkage, matrix−fracture mechanical interactions, and shale bulk strain influenced by matrix swelling/shrinkage. The last two items are governed by swelling/shrinkage behaviors. Once the swelling/shrinkage is uniform, the sorption items in eq 17 cancel each other out. In this case, eq 17 would degenerate into the solution of existing conventional models, where permeability is only related to effective stress changes.

2.4. Gas Flow in Matrices. As mentioned above, the shale matrix typically consists of two primary components: organic matrix and inorganic matrix. In the two components, gas storage modes and flow processes are distinct.[38,40] Therefore, in formulating the governing equation for gas flow in a matrix, it is essential to individually consider storage patterns and flow mechanisms within these two components, while also factoring in their respective proportions. According to eqs 2 and 3, the weight coefficient ω that defines the proportion of organic matter to the total matrix could be determined. Based on the weight coefficient and the mass conservation law, gas flow in the matrix is defined as

$$\frac{\partial}{\partial t_g}(\omega m_{gom} + (1-\omega)m_{gim}) + \nabla\cdot J_{gm} = \frac{k_{gm_{app}}\rho_{gm}}{\mu}\psi(p_{gf} - p_{gm}) \tag{18}$$

where m_{gom} refers to the gas mass in the organic matrix, m_{gim} refers to the gas mass in the inorganic matrix, and J_{gm} is the mass flux. The gas mass in these two components is

$$m_{gom} = \varphi_{gom}\rho_{gm} + \rho_{ga}\rho_{om}\frac{V_{Lom}p_{gm}}{p_{gm} + p_L} \tag{19}$$

$$m_{gim} = \varphi_{gim}\rho_{gm} + \rho_{ga}\rho_{im}\frac{V_{lim}p_{gm}}{p_{gm} + p_L} \tag{20}$$

where φ_{gom} is the porosity in the organic matrix; ρ_{om} is the density of the organic matrix; V_{Lom} is the Langmuir's volume constant for the organic matrix; φ_{gim} is the porosity in the inorganic matrix; ρ_{im} is the density of the inorganic matrix; and V_{Lim} is the Langmuir's volume constant for the inorganic matrix.

The gas flux in the matrix should be the sum of the gas flux in organic and inorganic parts. Therefore, according to the proportion of the two matrix components, it can be written as

$$J_{gm} = \omega J_{om} + (1-\omega)J_{im} \tag{21}$$

where J_{om} is the mass flux in the organic matrix and J_{im} is the mass flux in the inorganic matrix.

In shale matrix, whether organic or inorganic matter, the pore size is tiny with diameters in the nanometre range.[63−65] This means that the pore diameter is typically close to the

https://doi.org/10.1021/acs.energyfuels.3c03774
Energy Fuels 2024, 38, 1083−1097

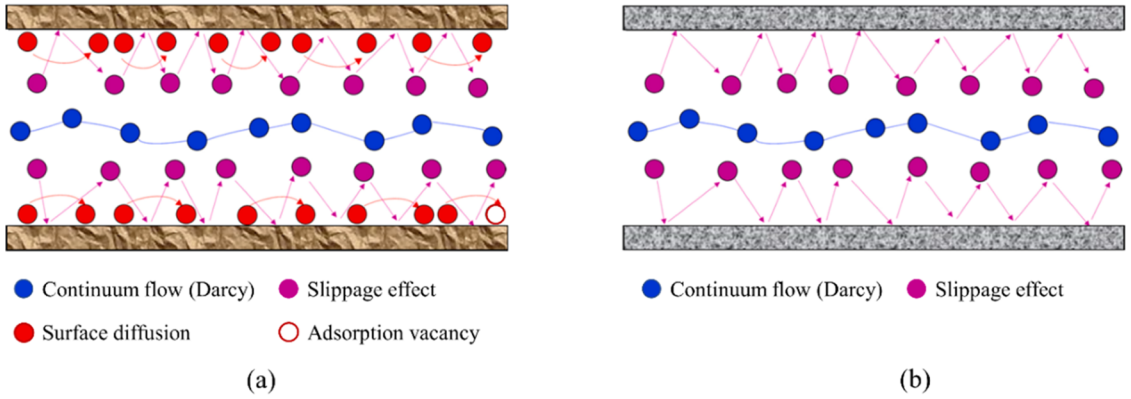

Figure 4. Illustration of flow mechanisms in the matrix: (a) organic matrix and (b) inorganic matrix.

mean free path of gas, and the collision frequency between gas molecules and pore walls becomes larger.[5,12,66] In this case, the traditional continuum flow governed by Darcy's law is no longer applicable, and flow regimes also play an important role in gas transport. Therefore, relying solely on intrinsic permeability (related to Darcy's law) is insufficient to accurately describe gas flow characteristics. Instead, apparent permeability, consisting of intrinsic permeability and the correction factor reflecting the influence of flow regimes, is generally employed[16]

$$k_{app} = k_{int} f(Kn) \tag{22}$$

where k_{app} is the apparent permeability; k_{int} is the intrinsic permeability; and $f(Kn)$ is the correction factor that is a function of the Knudsen number and is given by

$$f(Kn) = (1 + \xi Kn)\left(1 + \frac{4Kn}{1 + Kn}\right) \tag{23}$$

where ξ is the dimensionless rarefaction coefficient. This coefficient is determined by the Knudsen number[67]

$$\xi = \frac{128}{15\pi^2}\tan^{-1}(4Kn^{0.4}) \tag{24}$$

Flow regimes are determined by the Knudsen number, which is a function of the ratio between the molecular mean free path and pore radius. In general, flow regimes in organic and inorganic parts are the slip flow.[8,68] However, given that the pore radius within organic matter is much smaller, the impact of flow regimes on gas flow characteristics within it would be more pronounced.[40] Moreover, due to the presence of a large amount of adsorbed gas within the organic matrix, it is also necessary to consider its internal occurring diffusion of adsorbed gas along pore walls from high to low concentration (known as surface diffusion).[69] Consequently, the gas flow mechanism within an organic matrix involves both the slip flow and surface diffusion, while within an inorganic matrix, it is primarily governed by the slip flow alone, as illustrated in Figure 4.

The mass flux in the inorganic matrix can be described as a modified Darcy equation[15]

$$J_{im} = -\rho_{gm}\frac{k_{gim_{app}}}{\mu}\nabla p_{gm} \tag{25}$$

where $k_{gim_{app}}$ is the apparent permeability for an inorganic matrix, which can be expressed as

$$k_{gim_{app}} = k_{gim_{int}}(1 + \xi_{gim}Kn_{gim})\left(1 + \frac{4Kn_{gim}}{1 + Kn_{gim}}\right) \tag{26}$$

The Knudsen number in the inorganic matrix is

$$Kn_{gim} = \frac{\lambda_m}{r_{im}} \tag{27}$$

In this study, we assume that the porosity and intrinsic permeability for both the organic and inorganic matrix remain constant. In this case, it is reasonable to consider the pore radius within these two matrix components to keep unchanged as well, given the relationship between the pore radius, porosity, and intrinsic permeability.[70]

The mean free path is given by

$$\lambda_m = \frac{K_B T}{\sqrt{2}\,\pi\tilde{\sigma}^2 p_{gm}} \tag{28}$$

where K_B is the Boltzmann constant; T is the temperature; and $\tilde{\sigma}$ is the collision diameter for gas molecules.

The mass flux in the organic matrix can be expressed as the sum of two terms: the slip flow term ($J_{om_{slip}}$) and the surface diffusion term ($J_{om_{sur}}$)

$$J_{om} = J_{om_{slip}} + J_{om_{sur}} \tag{29}$$

The slip flow term can also be written as a modified Darcy equation

$$J_{om_{slip}} = -\rho_{gm}\frac{k_{gom_{app}}}{\mu}\nabla p_{gm} \tag{30}$$

where $k_{gom_{app}}$ is the apparent permeability of the organic matrix, which can be expressed as

$$k_{gom_{app}} = k_{gom_{int}}(1 + \xi_{gom}Kn_{gom})\left(1 + \frac{4Kn_{gom}}{1 + Kn_{gom}}\right) \tag{31}$$

The Knudsen number is given by

$$Kn_{gom} = \frac{\lambda_m}{r_{om}} \tag{32}$$

The mass flux of surface diffusion in the organic matrix is[21]

$$J_{om_{sur}} = -D_{gom}\nabla C_{gom} \tag{33}$$

https://doi.org/10.1021/acs.energyfuels.3c03774
Energy Fuels 2024, 38, 1083−1097

where D_{gom} is the surface diffusion coefficient in the organic matrix and C_{gom} is the gas concentration, and based on the Langmuir-type equation, its expression is defined as

$$C_{gom} = \rho_{ga}\rho_{om}\frac{V_{Lom}p_{gm}}{p_{gm} + p_L} \tag{34}$$

The total mass flux in the matrix (J_{gm}) can also be written in terms of permeability and the pressure gradient

$$J_{gm} = -\rho_{gm}\frac{k_{gm_{app}}}{\mu}\nabla p_{gm} \tag{35}$$

After combining eqs 21−35, we can derive the matrix apparent permeability that takes into account different flow mechanisms in organic and inorganic matrixes as well as the proportion of each matrix component

$$k_{gm_{app}} = \omega k_{gom_{app}} + \omega D_{gom}\rho_{ga}\rho_{om}\frac{V_{Lom}p_L}{(p_{gm} + p_L)^2}\frac{\mu}{\rho_{gm}} + (1 - \omega)k_{gim_{app}} \tag{36}$$

2.5. Gas Flow in Hydraulic Fractures. Hydraulic fracturing has been an important technique for unlocking vast natural gas resources contained within shale formations. After fracking, a network of primary hydrofractures with millimeter-scale apertures is created. These primary fractures can stimulate gas production by increasing the surface area available for gas to flow through, as well as reducing the flow resistance.[71,72] In hydraulic fractures, the effects of gas sorption and flow regimes are generally ignored, and Darcy's law is employed to describe gas flow characteristics. Therefore, the governing equation for gas flow in hydraulic fractures is given by

$$\frac{\partial}{\partial t_g}(\varphi_{ghf}\rho_{ghf}) + \nabla_T\left(-\rho_{ghf}\frac{k_{ghf}}{\mu}\nabla p_{ghf}\right) = 0 \tag{37}$$

where φ_{ghf} is the porosity of hydraulic fractures; ρ_{ghf} is the gas density in hydraulic fractures; k_{ghf} is the permeability of hydraulic fractures; and ∇_T denotes the tangential component of the gradient operator, which can be used to describe the pressure gradient in the tangential plane of hydraulic fractures.

The porosity and permeability of hydraulic fractures can be expressed as[5,68]

$$\frac{\varphi_{ghf}}{\varphi_{ghf_0}} = \exp(-c_{ghf}(p_{ghf_0} - p_{ghf})) \tag{38}$$

$$\frac{k_{ghf}}{k_{ghf_0}} = \exp(-3c_{ghf}(p_{ghf_0} - p_{ghf})) \tag{39}$$

where c_{ghf} is the compressibility for hydraulic fractures.

3. MODEL VERIFICATION

In this section, in order to validate the proposed concepts and models, simulation results are compared with both measurements obtained in the laboratory and production data in the field. The proposed equations and models are solved by COMSOL Multiphysics, which provides a powerful Multiphysics modeling environment based on the finite element method.

3.1. Comparison with Long-Term Experimental Observations. To monitor the dynamic evolution of permeability under nonequilibrium states, it is essential to continuously collect permeability data during the experimental process (called long-term laboratory tests). In this part, the simulation results would be compared with observations from a long-term test. In this experiment, confining and injection pressure are maintained constant at 9 and 5 MPa, respectively, and permeability data are collected at six different time points after gas injection.[73] As shale samples lack hydraulic fractures, the governing equation for gas flow within such fractures is ignored. Furthermore, due to the existence of noticeable natural fractures on samples, with fracture permeability typically exceeding matrix permeability by several orders of magnitude, the obtained permeability data are considered as fracture permeability. In order to highlight the influence of the matrix nonuniform swelling, the results calculated by a conventional model based on the uniform RVE are compared.[5] The parameters used in the simulation are listed in Table 1.

Table 1. Simulation Parameters Used for Experimental Observations

parameter	value
initial natural fracture porosity, φ_{gf_0}	0.005
inorganic matrix porosity, φ_{gim}	0.05
organic matrix porosity, φ_{gom}	0.09
bulk modulus of fracture, K_f	100 [MPa]
dynamic viscosity, μ	6×10^{-5} [Pa/s^{-1}][35]
intrinsic permeability for organic matrix, $k_{gom_{int}}$	4.8×10^{-22} [m^2]
intrinsic permeability for inorganic matrix, $k_{gim_{int}}$	1×10^{-21} [m^2]
initial permeability for natural fracture, k_{gf_0}	1×10^{-17} [m^2]
shale density, ρ_s	2500 [kg/m^3][68]
Langmuir's strain constant, ε_L	0.005
Langmuir's volume constant for fracture, V_{Lf}	0.004 [m^3/kg]
Langmuir's volume constant for organic matrix, V_{Lom}	0.015 [m^3/kg]
Langmuir's volume constant for inorganic matrix, V_{Lim}	0.004 [m^3/kg]
Langmuir's pressure constant, p_L	3 [MPa]
Boltzmann constant, K_B	1.38×10^{-23} [J/K][5]
temperature, T	300 [K][73]
collision diameter, $\tilde{\sigma}$	0.42 [nm][5]
surface diffusion coefficient, D_{gom}	1×10^{-8} [m^2/s][5]
shape factor, ψ	4000 [m^{-2}]
gas density at standard state, ρ_{ga}	0.75 [kg/m^3][68]
initial pressure, p_i	0.1 [MPa][73]
gas compressibility, c_t	3.42^{-8}[Pa^{-1}]
matrix size, L	0.05 [m]

The comparison between the simulation results and experimental ones is shown in Figure 5. It is evident that the calculations from the proposed models are in good agreement with the experimental data. In contrast, there is a significant deviation from the results of the conventional model. In order to better explain the role of the matrix nonuniform swelling in the fracture permeability evolution, swelling paths at four moments and the evolution of the nonuniform swelling coefficient from the beginning to the end are plotted in Figure 6. It is evident that during the first 200 s after gas injection, the nonuniform swelling coefficient remains unchanged, which indicates that gas has not yet invaded into matrix. In this case, the matrix swelling is not involved in the fracture permeability evolution, and the results of these two models are basically

https://doi.org/10.1021/acs.energyfuels.3c03774
Energy Fuels 2024, 38, 1083−1097

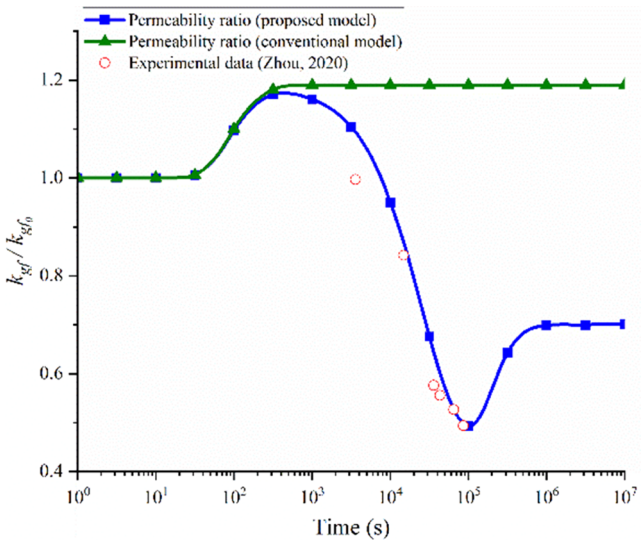

Figure 5. Comparison between simulation results and experimental observations.

consistent. However, following this point, there is a marked difference in their calculations. After gas invasion into the matrix, swelling behaviors would change. Initially, gas primarily invades the area near the fracture wall, and the gas adsorption-induced swelling is also localized in that specific area. Under this condition, swelling behaviors are close to the localized case, and thus, the nonuniform swelling coefficient drops. This implies that matrix swelling would mostly contribute to fractures, leading to fracture compression and a subsequent reduction in permeability. With the progression of diffusion, gas is no longer only confined to the vicinity of the fracture wall but permeates the whole matrix, and the associated swelling follows the same pattern. In this case, the swelling path gradually converges to the diagonal, and the coefficient begins to rebound. Therefore, the proportion of the matrix swelling acting on fractures decreases, resulting in a rebound in permeability. When gas diffusion is complete, the pressure becomes uniformly distributed throughout the whole matrix, and the nonuniform swelling coefficient reverts to its initial value before the gas invasion. Nevertheless, due to the compositional heterogeneity, even at equilibrium matrix still does not swell uniformly, and thus, the nonuniform swelling coefficient remains below unity.

3.2. Comparison with Field Production Data. In this section, the calculation results of the proposed models are compared with the production data from North American reservoirs (Marcellus Shale and Barnett Shale). Due to boundary symmetry, a quarter of these two reservoirs are used to construct the physical model, thereby reducing the computational cost. The geometry and boundary conditions are plotted in Figure 7. Hydraulic fractures are represented by 1-D lines, while natural fractures and matrixes are represented by two overlapping continuums. Furthermore, in situ stresses are simplified as orthogonal maximum and minimum horizontal stresses (held unchanged during gas production). The simulation parameters for the Marcellus Shale and the Barnett Shale are listed in Table 2.

The comparison between the simulation results and the on-site production data is plotted in Figure 8. It is apparent that the predictions of the proposed models can be well matched with filed data, which indicates their accuracy and reliability. In the case of the Marcellus Shale, following depressurization, the gas production rate decreases from its peak value of 9.1×10^4 m^3/d to a mere 2.7×10^4 m^3/d within a span of 270 days. In the initial stage, the calculated results are slightly higher than the field data. This disparity could be attributed to the fact that, in the course of the actual production process, the flow back of water after hydraulic fracturing might result in slight blockages and a subsequent decrease in permeability. However, the proposed models do not account for this phenomenon. For the Barnett Shale, after the initiation of production, the production rate first experiences a rapid increase and reaches its peak within the first 10 days. However, in the subsequent 600 days, it exhibits a sharp decline trend, plummeting from 2.13×10^5 m^3/d to 3×10^4 m^3/d, a drop of almost 90%. After that, the decline rate decelerates considerably, and the production rate only further declines to 1.2×10^4 m^3/d over the remaining 900 days. It can be observed that gas productivity from the Barnett Shale significantly surpasses that from the Marcellus Shale despite the latter having a higher reservoir pressure. This is because the number of hydraulic fractures in the Barnett Shale is twice that in the Marcellus Shale. Therefore, it can be inferred that hydraulic fracturing plays a crucial role in enhancing shale gas production.

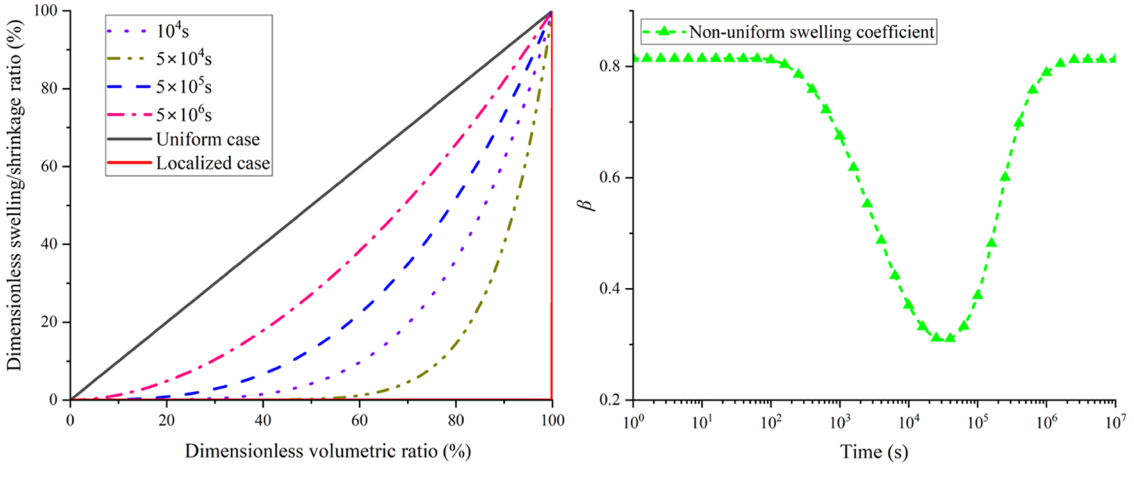

Figure 6. Evolution of the swelling path and nonuniform swelling coefficient.

https://doi.org/10.1021/acs.energyfuels.3c03774
Energy Fuels 2024, 38, 1083−1097

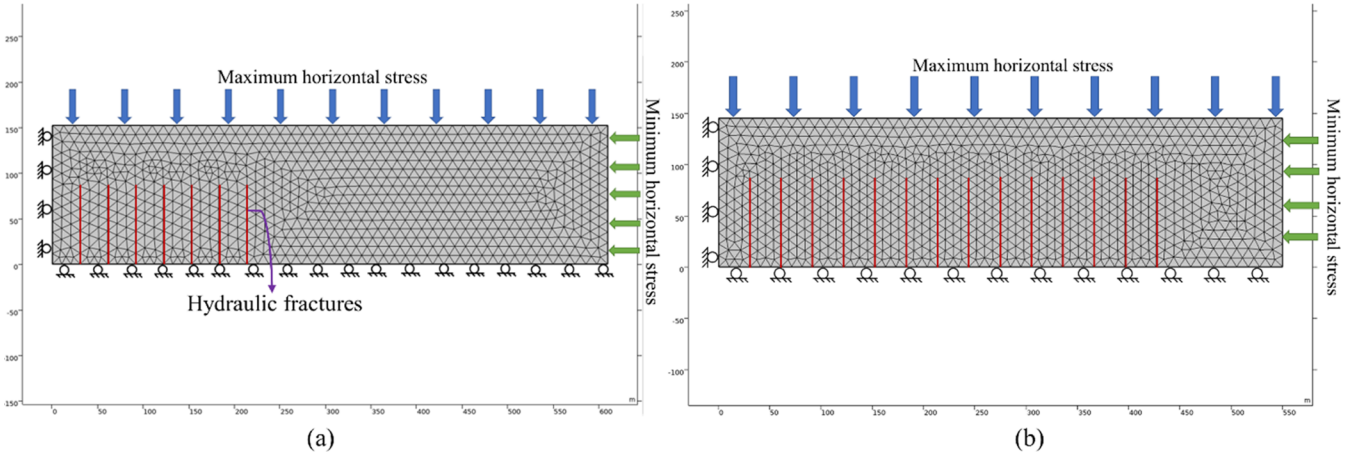

Figure 7. Geometry and boundary conditions for reservoirs: (a) Marcellus Shale and (b) Barnett Shale.

Table 2. Simulation Parameters Used for Field Data

parameter	Marcellus Shale	Barnett Shale
geological model dimension	609.6 [m] × 152.4 [m] × 52.7 [m][68]	550 [m] × 145[m] × 90 [m][68]
initial hydraulic fracture porosity, φ_{ghf_0}	0.2[68]	0.2[68]
initial natural fracture porosity, φ_{gf_0}	0.02	0.02
inorganic matrix porosity, φ_{gim}	0.04	0.03
Organic matrix porosity, φ_{gom}	0.08	0.05
maximum horizontal stress	42 [MPa][5]	41.6 [MPa][5]
minimum horizontal stress	37.2 [MPa][5]	37.3 [MPa][5]
hydraulic fracture compressibility, c_{ghf}	1×10^{-8} [Pa^{-1}]	1×10^{-8} [Pa^{-1}]
dynamic viscosity, μ	2×10^{-5} [Pa/s^{-1}][5]	2×10^{-5} [Pa/s^{-1}][5]
intrinsic organic matrix permeability, $k_{gom_{int}}$	4.6×10^{-21} [m^2]	7.5×10^{-21} [m^2]
intrinsic inorganic matrix permeability, $k_{gim_{int}}$	2.5×10^{-20} [m^2]	4.8×10^{-20} [m^2]
initial natural fracture permeability, k_{gf_0}	1×10^{-17} [m^2]	3.8×10^{-17} [m^2]
initial hydraulic fracture permeability, k_{ghf_0}	8×10^{-14} [m^2]	8×10^{-14} [m^2]
shale density, ρ_s	2500 [kg/m^3][68]	2500 [kg/m^3][68]
Langmuir's strain constant, ε_L	0.005	0.005
Langmuir's volume constant for fractures, V_{Lf}	0.003 [m^3/kg]	0.002 [m^3/kg]
Langmuir's volume constant for organic matrix, V_{Lom}	0.01 [m^3/kg]	0.008 [m^3/kg]
Langmuir's volume constant for inorganic matrix, V_{Lim}	0.003 [m^3/kg]	0.002 [m^3/kg]
Langmuir's pressure constant, p_L	3 [MPa][5]	4.8 [MPa][5]
Boltzmann constant, K_B	1.38×10^{-23} [J/K][5]	1.38×10^{-23} [J/K][5]
temperature, T	353 [K][68]	353 [K][68]
collision diameter, $\tilde{\sigma}$	0.38 [nm][40]	0.38 [nm][40]
surface diffusion coefficient, D_{gom}	1×10^{-8} [m^2/s][5]	1×10^{-8} [m^2/s][5]
shape factor, ψ	4000 [m^{-2}]	4000 [m^{-2}]
gas density at standard conditions, ρ_{ga}	0.717 [kg/m^3][68]	0.717 [kg/m^3][68]
initial reservoir pressure	34.5 [MPa][5]	20.34 [MPa][5]
bottom hole pressure	2.4 [MPa][5]	3.69 [MPa][5]

4. MODEL APPLICATIONS AND ANALYSIS

In this section, the established models are applied as a benchmark to conduct a series of parametric analyses. This contributes to a more profound comprehension of gas flow characteristics and gas production under the influence of gas diffusion and the dispersed distribution of organic matter within an inorganic matrix.

4.1. Influence of Matrix Nonuniform Shrinkage on Gas Production. To examine the role of the matrix nonuniform shrinkage during gas production, in this part, the developed models are applied to real-world field scenarios, and two cases are introduced. In one case, β is determined by the transient process and complex structure, while in the other, β is assigned a constant value of 1, corresponding to uniform shrinkage. The gas production rate and cumulative gas production for these two cases are plotted in Figure 9a. Apparently, following depressurization, for both cases, the gas production rate first reaches the peak value almost instantaneously and then experiences a trend of sharp decrease. However, the decline rates in the two cases are not the same, resulting in different forecasts of cumulative production. In general, neglecting the nonuniform shrinkage and its resulting consequences would lead to an underestimation of gas production rates and cumulative production. After a decade, the prediction for cumulative gas production that takes into account the impact of the matrix nonuniform shrinkage is 5.83

https://doi.org/10.1021/acs.energyfuels.3c03774
Energy Fuels 2024, 38, 1083−1097

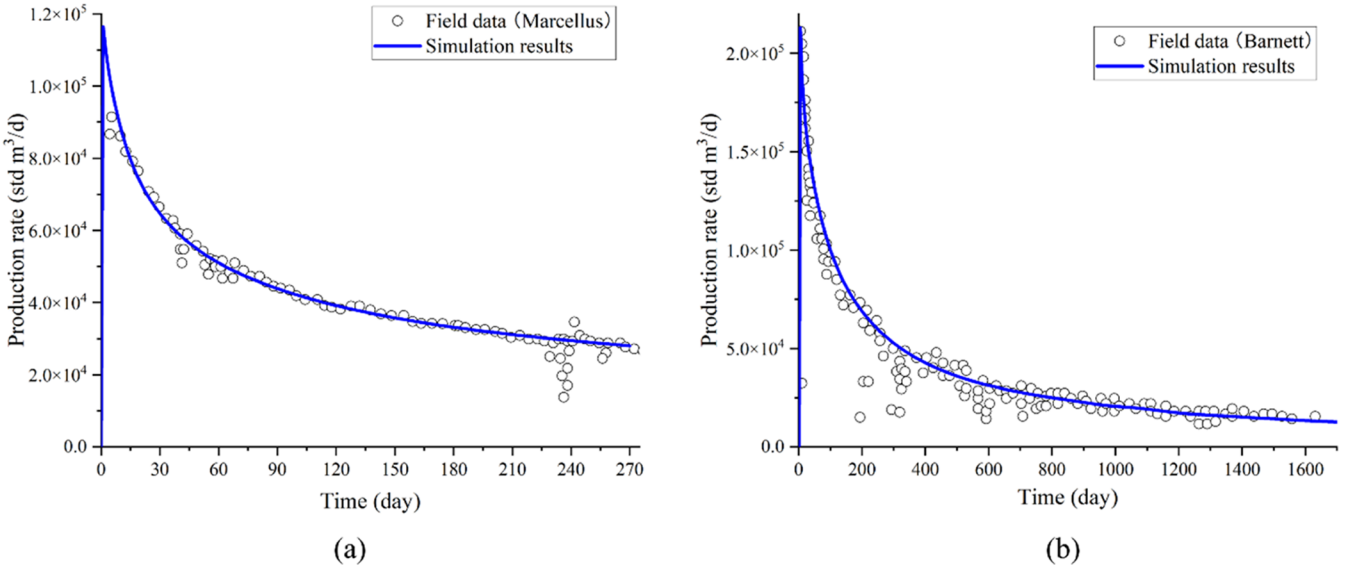

Figure 8. Comparison between simulation results and gas production data: (a) Marcellus Shale and (b) Barnett Shale.

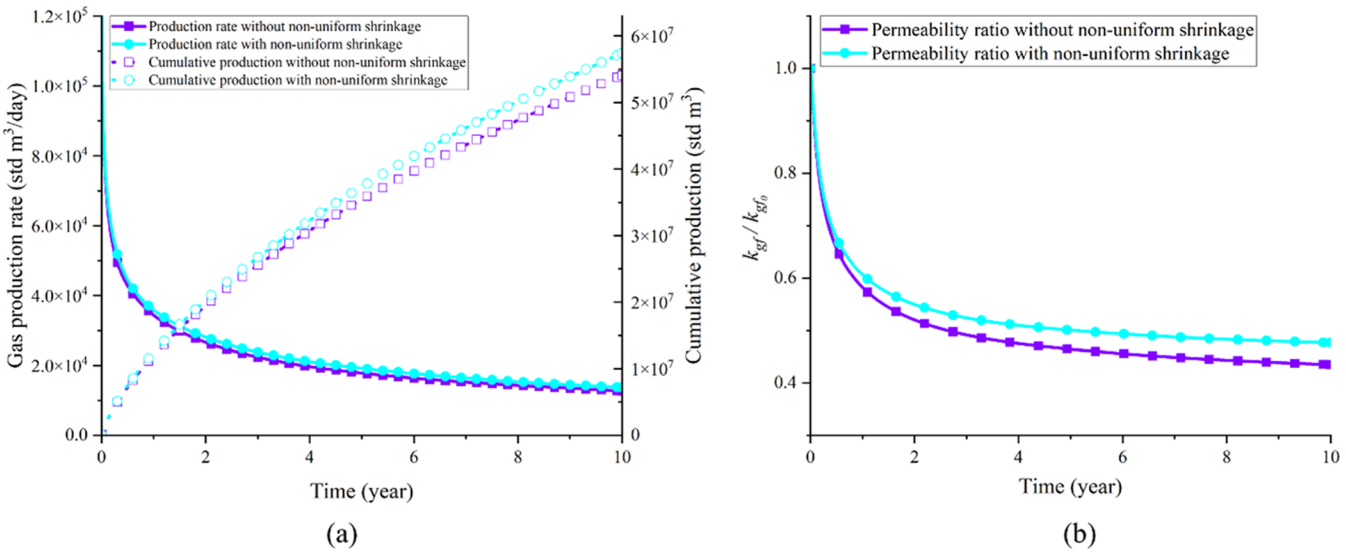

Figure 9. Effects of matrix nonuniform shrinkage on gas production and shale permeability: (a) gas production rate and cumulative production and (b) nature fracture permeability ratio.

$\times 10^7$ m^3, which is approximately 1.1 times higher than that without the consideration of this impact. The main reason for this discrepancy is that shale fracture permeability would be underestimated when the nonuniform shrinkage is neglected, as shown in Figure 9b. As gas is produced, the reservoir pressure would continue to decrease, causing an increase in the effective stress. The elevated stress results in fracture compression and a reduction in the fracture permeability. As a result, the permeability in both cases shows a declining trend. However, the decrease in permeability induced by the pressure reduction would be balanced by the matrix−fracture mechanical interactions resulting from the matrix nonuniform shrinkage. Consequently, when the influence of the nonuniform shrinkage is taken into account, the downward trend in permeability would be mitigated. In this case, gas can flow more quickly to the wellbore and be produced.

4.2. Difference in Degree of Nonuniform Swelling/Shrinkage during Gas Injection and Production. From eq 17, it can be seen that shale fracture permeability is influenced by the nonuniform swelling coefficient, which serves as an indicator for the degree of the nonuniform swelling/shrinkage. During gas injection, gas propagates from the fracture wall to the inner matrix, whereas during gas production, gas diffuses from deeper matrix regions toward fractures. This implies that in the two processes, the pressure distribution in the matrix is distinct, which leads to a difference in the degree of the nonuniform swelling/shrinkage. As a result, the extent to which resulting matrix−fracture mechanical interactions impact permeability would also be distinct. In this section, this difference in the degree of the nonuniform swelling/shrinkage is explored by simulating both gas injection and extraction on the same sample. All parameters remain consistent except for initial pressure and boundary conditions. It should be noted that in this part, we solely focus on the effect of gas diffusion. Consequently, the dispersed distribution of organic matter is disregarded, that is, Langmuir's strain constant in the matrix is assumed to be uniform in the local embedded RVE. The difference is characterized by comparing

https://doi.org/10.1021/acs.energyfuels.3c03774
Energy Fuels 2024, 38, 1083−1097

the evolutions of the nonuniform swelling coefficient during gas injection and production, as shown in Figure 10. It is

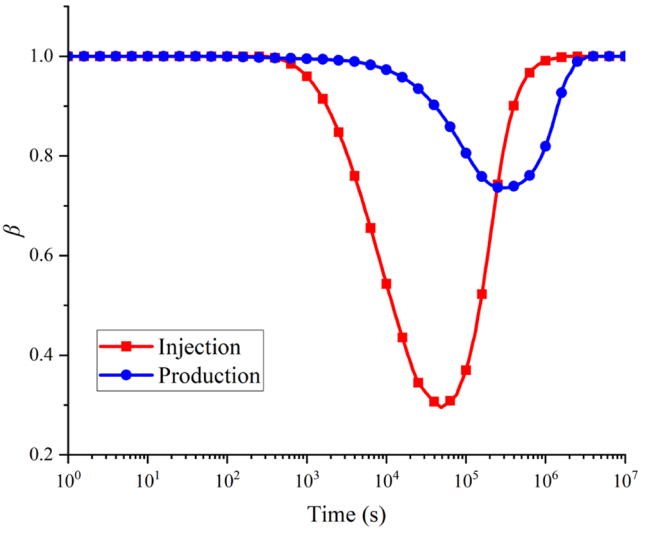

Figure 10. Evolution of the nonuniform swelling coefficient during gas injection and production.

evident that the drop in the nonuniform swelling coefficient during gas injection is more evident (occurring earlier and exhibiting a larger magnitude) compared to gas production. This means that in terms of the degree of nonuniformity alone, it is significantly greater in the gas injection process compared to the gas extraction process. The varying evolution of the nonuniform swelling coefficient suggests that the role of the nonuniform swelling/shrinkage should be analyzed separately for gas injection and production. In general, the gas sorption effect during gas injection plays a more important role than that during gas production.

4.3. Influence of Flow Regimes on Swelling/Shrinkage Behaviors. Gas diffusion in the matrix is closely related to matrix permeability, the magnitude of which dictates the speed of gas propagation through the matrix. As shown in eq 22, flow regimes have a significant effect on matrix permeability. In this section, we discuss the influence of flow regimes on gas diffusion and corresponding swelling/shrinkage behaviors. Two scenarios are established: one considers matrix permeability as apparent permeability (with flow regime effects), while the other considers it solely as intrinsic permeability (without flow regime effects). Figures 11 and 12 present the evolution of matrix permeability and the nonuniform swelling coefficient for the two scenarios during gas injection and production, respectively. It is evident that during gas injection when the influence of flow regimes is incorporated, matrix permeability would be boosted significantly in the early stage, while the impact of flow regimes on matrix permeability during gas production mainly manifests in the later stage. This is because an increase in pressure leads to a decrease in the average free path of gas molecules, consequently diminishing the probability of collisions between gas molecules and pore walls. Under these conditions, the Knudsen number decreases, and the influence of flow regimes becomes minor. For gas injection, gas is able to quickly invade the matrix in the initial stage when considering flow regime effects. Consequently, swelling behaviors would approach the localized case more quickly, leading to a greater decline rate of the nonuniform swelling coefficient. However, flow regimes play a minor role in the evolution of the swelling path from the perpendicular boundaries to the diagonal. For gas production, the opposite is true; that is, flow regimes have a minimal effect on the initial evolution of shrinkage behaviors toward the localized case but significantly affect its subsequent evolution toward the uniform case.

4.4. Influence of Proportion of the Organic Matrix. From eqs 25−36, it is conspicuous that gas flow characteristics in organic and inorganic matrices are different and that the proportion of these two matrix components control matrix apparent permeability. Therefore, in this part, through varying the shape parameter in eq 3, the local embedded RVEs with various proportions of organic matter are generated to explore the influence of its proportion on matrix permeability. The variation in matrix permeability with the proportion under different pressures is plotted in Figure 13. It is evident that with an increase in the proportion of organic matrix, permeability changes can be divided into two categories. At low pressure (<1 MPa), matrix permeability increases with

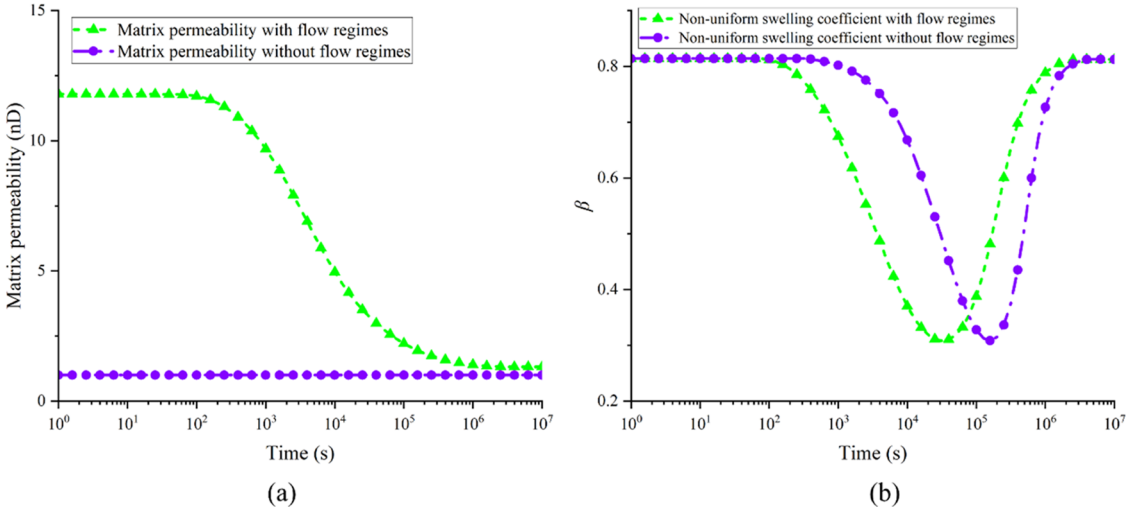

Figure 11. Influence of flow regimes on matrix permeability and swelling behaviors during gas injection: (a) matrix permeability and (b) nonuniform swelling coefficient.

https://doi.org/10.1021/acs.energyfuels.3c03774
Energy Fuels 2024, 38, 1083−1097

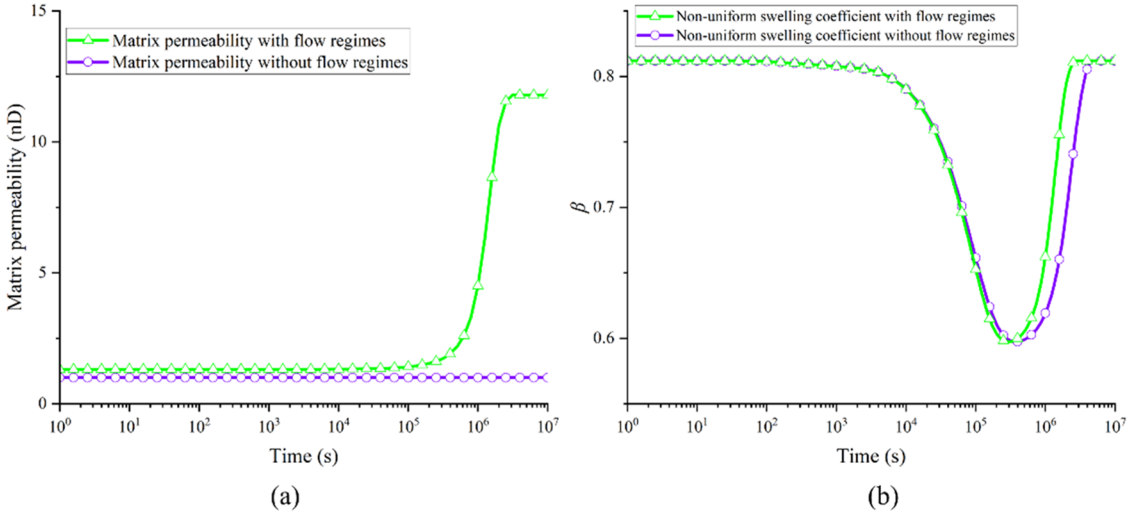

Figure 12. Influence of flow regimes on matrix permeability and shrinkage behaviors during gas production: (a) matrix permeability and (b) nonuniform swelling coefficient.

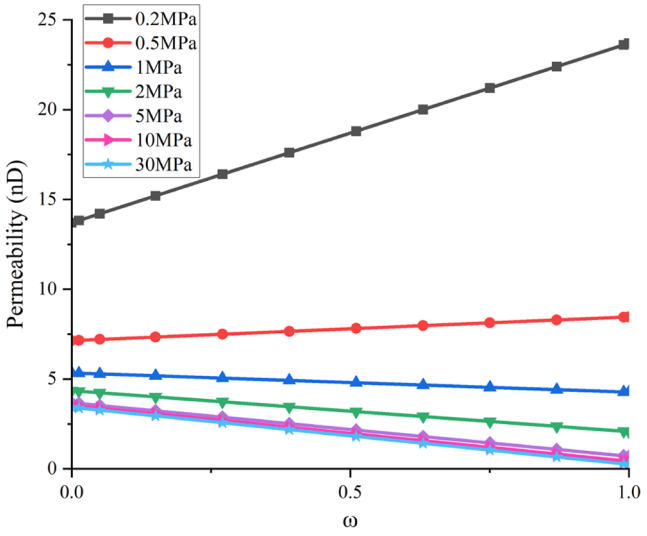

Figure 13. Influence of the proportion of organic inclusions on matrix permeability.

organic inclusions, while at high pressure (≥1 MPa), the opposite trend is presented. This implies that the slip flow and surface diffusion in an organic matrix have a great contribution to matrix permeability at low pressure, whereas gas flow in an inorganic matrix plays an important role at high pressure. This is because pores with diameters below 50 nm are predominantly distributed in the organic matrix, while pores with diameters above 50 nm are more easily observed in the inorganic matrix.[40,63] In this case, gas flow in an organic matrix is more sensitive to changes in flow regimes. As a consequence, the apparent permeability for the organic matrix is larger than that for the inorganic matrix at low pressure. However, at high pressure, the influence of surface diffusion and the slip flow would be minor, and thus, intrinsic permeability would play a decisive role. In general, the intrinsic permeability for the organic matrix is much lower than that for the inorganic matrix.[12]

5. CONCLUSIONS

In this study, the influence of gas diffusion and the dispersed distribution of organic matter in an inorganic matrix on shale gas flow characteristics and gas production is discussed. Through the concept of the swelling path and swelling triangle, the role of the nonuniform swelling/shrinkage induced by the transient process and complex structure in shale fracture permeability is investigated. Furthermore, the effects of different flow mechanisms in organic and inorganic matrixes, as well as the proportion of these two matrix components on shale matrix permeability, are explored. Based on our research, the following conclusions can be drawn:

- When aiming to predict gas production rates and cumulative production in the field, models that ignore the impact of the transient process and complex structure demonstrate substantial bias. In these models, the important data tend to be underestimated due to inaccurate permeability estimations.
- The flow regime effect in the matrix would change the gas diffusion process and thus affect swelling/shrinkage behaviors. During gas injection, this effect accelerates the approach of the swelling path toward the two perpendicular boundaries of the swelling triangle while exerting a minimal impact on its subsequent evolution from the perpendicular boundaries to the diagonal, while during gas production, the opposite is true.
- During gas injection and production, the pressure distribution exhibits different trends, leading to various degrees of nonuniform swelling/shrinkage. In this case, the influence of matrix−fracture mechanical interactions is also different. Specifically, the mechanical interactions during gas injection have a more pronounced effect on shale fracture permeability compared to those during gas production.
- Gas flow in inorganic and organic matrices is governed by different mechanisms, and matrix permeability is closely tied to the proportion of these two matrix components. In general, at low pressure, an increase in organic matter tends to enhance matrix permeability, whereas at high pressure, a greater proportion of organic matrix corresponds to decreased matrix permeability.

https://doi.org/10.1021/acs.energyfuels.3c03774
Energy Fuels 2024, 38, 1083−1097

AUTHOR INFORMATION

Corresponding Author

Yifan Huang − *Department of Chemical Engineering, School of Engineering, The University of Western Australia, Crawley, Western Australia 6009, Australia;* orcid.org/0000-0002-6020-2240; Email: yifan.huang@research.uwa.edu.au

Authors

Jishan Liu − *Department of Chemical Engineering, School of Engineering, The University of Western Australia, Crawley, Western Australia 6009, Australia;* orcid.org/0000-0002-2744-0319

Qi Gao − *Department of Chemical Engineering, School of Engineering, The University of Western Australia, Crawley, Western Australia 6009, Australia*

Derek Elsworth − *Department of Energy and Mineral Engineering, G3 Centre and Energy Institute, The Pennsylvania State University, University Park, Pennsylvania 16802, United States*

Yee-Kwong Leong − *Department of Chemical Engineering, School of Engineering, The University of Western Australia, Crawley, Western Australia 6009, Australia;* orcid.org/0000-0002-5616-1618

Complete contact information is available at: https://pubs.acs.org/10.1021/acs.energyfuels.3c03774

Notes

The authors declare no competing financial interest.

ACKNOWLEDGMENTS

This work is supported by the Australian Research Council under Grant DP200101293. The first author is supported by the UWA−China Joint Scholarships (201906430030). These supports are gratefully acknowledged.

REFERENCES

(1) Feng, Y. Y.; Zhang, L. X. Scenario analysis of urban energy saving and carbon abatement policies: a case study of Beijing city, China. *Procedia Environ. Sci.* **2019**, *13*, 632−644.

(2) Aydin, G.; Jang, H.; Topal, E. Energy consumption modeling using artificial neural networks: The case of the world's highest consumers. *Energy Sources, Part B* **2016**, *11* (3), 212−219.

(3) *Annual Energy Outlook 2010*, U.S. Energy Information Administration20101-15.

(4) Mistré, M.; Crénes, M.; Hafner, M. Shale gas production costs: historical developments and outlook. *Energy Strategy Rev.* **2018**, *20*, 20−25.

(5) Cao, P.; Liu, J.; Leong, Y. K. A fully coupled multiscale shale deformation-gas transport model for the evaluation of shale gas extraction. *Fuel* **2016**, *178*, 103−117.

(6) Zeng, J.; Liu, J.; Li, W.; Leong, Y. K.; Elsworth, D.; Guo, J. Evolution of shale permeability under the influence of gas diffusion from the fracture wall into the matrix. *Energy Fuels* **2020**, *34* (4), 4393−4406.

(7) Taghavinejad, A.; Sharifi, M.; Heidaryan, E.; Liu, K.; Ostadhassan, M. Flow modeling in shale gas reservoirs: A comprehensive review. *J. Nat. Gas Sci. Eng.* **2020**, *83*, No. 103535.

(8) Cui, G.; Liu, J.; Wei, M.; Feng, X.; Elsworth, D. Evolution of permeability during the process of shale gas extraction. *J. Nat. Gas Sci. Eng.* **2018**, *49*, 94−109.

(9) Li, J.; Yu, T.; Liang, X.; Zhang, P.; Chen, C.; Zhang, J. Insights on the gas permeability change in porous shale. *Adv. Geo-Energy Res.* **2017**, *1* (2), 69−73.

(10) Javadpour, F. Nanopores and apparent permeability of gas flow in mudrocks (shales and siltstone). *J. Can. Pet. Technol.* **2009**, *48* (08), 16−21.

(11) Zhao, J.; Sun, M.; Pan, Z.; Liu, B.; Ostadhassan, M.; Hu, Q. Effects of pore connectivity and water saturation on matrix permeability of deep gas shale. *Adv. Geo-Energy Res.* **2022**, *6* (1), 54−68.

(12) Gao, Q.; Liu, J.; Leong, Y. K.; Elsworth, D. A Review of Swelling Effect on Shale Permeability: Assessments and Perspectives. *Energy Fuels* **2023**, *37* (5), 3488−3500.

(13) Huang, Y.; Liu, J.; Elsworth, D.; Leong, Y. K. A transient dual porosity/permeability model for coal multiphysics. *Geomech. Geophys. Geo-Energy GeoResour.* **2022**, *8* (2), No. 40.

(14) Berre, I.; Doster, F.; Keilegavlen, E. Flow in fractured porous media: a review of conceptual models and discretization approaches. *Transp. Porous Media* **2019**, *130* (1), 215−236.

(15) Peng, Y.; Liu, J.; Pan, Z.; Connell, L. D. A sequential model of shale gas transport under the influence of fully coupled multiple processes. *J. Nat. Gas Sci. Eng.* **2015**, *27*, 808−821.

(16) Javadpour, F.; Fisher, D.; Unsworth, M. Nanoscale gas flow in shale gas sediments. *J. Can. Pet. Technol.* **2007**, *46* (10), 55−61.

(17) Peng, Y.; Liu, J.; Wei, M.; Pan, Z.; Connell, L. D. Why coal permeability changes under free swellings: New insights. *Int. J. Coal Geol.* **2014**, *133*, 35−46.

(18) Liu, J.; Chen, Z.; Elsworth, D.; Miao, X.; Mao, X. Evolution of coal permeability from stress-controlled to displacement-controlled swelling conditions. *Fuel* **2011**, *90* (10), 2987−2997.

(19) Qu, H.; Liu, J.; Pan, Z.; Connell, L. Impact of matrix swelling area propagation on the evolution of coal permeability under coupled multiple processes. *J. Nat. Gas Sci. Eng.* **2014**, *18*, 451−466.

(20) Shi, R.; Liu, J.; Wang, X.; Elsworth, D.; Wang, Z.; Wei, M.; Cui, G. Experimental Observations of Gas-sorption-Induced Strain Gradients and their Implications on Permeability Evolution of Shale. *Rock Mech. Rock Eng.* **2021**, *54* (8), 3927−3943.

(21) Cui, G.; Xia-Ting, F.; Pan, Z.; Chen, T.; Liu, J.; Elsworth, D.; Tan, Y.; Wang, C. Impact of shale matrix mechanical interactions on gas transport during production. *J. Pet. Sci. Eng.* **2020**, *184*, No. 106524.

(22) Liu, J.; Chen, Z.; Elsworth, D.; Qu, H.; Chen, D. Interactions of multiple processes during CBM extraction: a critical review. *Int. J. Coal Geol.* **2011**, *87* (3−4), 175−189.

(23) Garum, M.; Glover, P. W.; Lorinczi, P.; Drummond-Brydson, R.; Hassanpour, A. Micro-and nano-scale pore structure in gas shale using Xμ-CT and FIB-SEM techniques. *Energy Fuels* **2020**, *34* (10), 12340−12353.

(24) Zeng, J.; Liu, J.; Guo, J. Characterization of gas transport in shale: A multi-mechanism permeability modeling approach. *Chem. Eng. J.* **2022**, *438*, No. 135604.

(25) Liu, K.; Ostadhassan, M.; Gentzis, T.; Carvajal-Ortiz, H.; Bubach, B. Characterization of geochemical properties and microstructures of the Bakken Shale in North Dakota. *Int. J. Coal Geol.* **2018**, *190*, 84−98.

(26) Huang, J.; Jin, T.; Barrufet, M.; Killough, J. Evaluation of CO2 injection into shale gas reservoirs considering dispersed distribution of kerogen. *Appl. Energy* **2020**, *260*, No. 114285.

(27) Ambrose, R. J.; Hartman, R. C.; Diaz-Campos, M.; Akkutlu, I. Y.; Sondergeld, C. H. Shale gas-in-place calculations part I: new pore-scale considerations. *SPE J.* **2012**, *17* (01), 219−229.

(28) Etminan, S. R.; Javadpour, F.; Maini, B. B.; Chen, Z. Measurement of gas storage processes in shale and of the molecular diffusion coefficient in kerogen. *Int. J. Coal Geol.* **2014**, *123*, 10−19.

(29) He, J.; Zhang, Y.; Li, X.; Wan, X. Experimental investigation on the fractures induced by hydraulic fracturing using freshwater and supercritical CO 2 in shale under uniaxial stress. *Rock Mech. Rock Eng.* **2019**, *52*, 3585−3596.

(30) Zeng, J.; Liu, J.; Li, W.; Leong, Y. K.; Elsworth, D.; Guo, J. Shale gas reservoir modeling and production evaluation considering complex gas transport mechanisms and dispersed distribution of kerogen. *Pet. Sci.* **2021**, *18*, 195−218.

(31) Zhang, H.; Liu, J.; Elsworth, D. How sorption-induced matrix deformation affects gas flow in coal seams: a new FE model. *Int. J. Rock Mech. Min. Sci.* **2008**, *45* (8), 1226−1236.
(32) Liu, X.; Chen, L.; Sheng, J.; Liu, J. A Non-Equilibrium multiphysics model for coal seam gas extraction. *Fuel* **2023**, *331*, No. 125942.
(33) Huang, Y.; Liu, J.; Zhao, Y.; Elsworth, D.; Leong, Y. K. Effect of non-uniform swelling on coal multiphysics during gas injection: The triangle approach. *J. Rock Mech. Geotech. Eng.* **2023**, DOI: 10.1016/j.jrmge.2023.06.008.
(34) Wei, M.; Liu, J.; Elsworth, D.; Li, S.; Zhou, F. Influence of gas adsorption induced non-uniform deformation on the evolution of coal permeability. *Int. J. Rock Mech. Min. Sci.* **2019**, *114*, 71−78.
(35) Cui, G.; Liu, J.; Wei, M.; Shi, R.; Elsworth, D. Why shale permeability changes under variable effective stresses: new insights. *Fuel* **2018**, *213*, 55−71.
(36) Wei, M.; Liu, J.; Elsworth, D.; Wang, E. Triple-porosity modelling for the simulation of multiscale flow mechanisms in shale reservoirs. *Geofluids* **2018**, *2018*, 1−11.
(37) Feng, Q.; Xu, S.; Wang, S.; Li, Y.; Gao, F.; Xu, Y. Apparent permeability model for shale oil with multiple mechanisms. *J. Pet. Sci. Eng.* **2019**, *175*, 814−827.
(38) Song, W.; Yao, J.; Li, Y.; Sun, H.; Zhang, L.; Yang, Y.; Zhao, J.; Sui, H. Apparent gas permeability in an organic-rich shale reservoir. *Fuel* **2016**, *181*, 973−984.
(39) Sheng, G.; Su, Y.; Zhao, H.; Liu, J. A unified apparent porosity/permeability model of organic porous media: Coupling complex pore structure and multimigration mechanism. *Adv. Geo-Energy Res.* **2020**, *4* (2), 115−125.
(40) Zhang, L.; Liang, H.; Zhao, Y.; Xie, J.; Peng, X.; Li, Q. Gas transport characteristics in shale matrix based on multiple mechanisms. *Chem. Eng. J.* **2020**, *386*, No. 124002.
(41) Wang, S.; Shi, J.; Wang, K.; Sun, Z.; Miao, Y.; Hou, C. Apparent permeability model for gas transport in shale reservoirs with nano-scale porous media. *J. Nat. Gas Sci. Eng.* **2018**, *55*, 508−519.
(42) Kouznetsova, V.; Geers, M. G.; Brekelmans, W. M. Multi-scale constitutive modelling of heterogeneous materials with a gradient-enhanced computational homogenization scheme. *Int. J. Numer. Methods Eng.* **2002**, *54* (8), 1235−1260.
(43) Li, B.; Benson, S. M. Influence of small-scale heterogeneity on upward CO2 plume migration in storage aquifers. *Adv. Water Resour.* **2015**, *83*, 389−404.
(44) Bertrand, F.; Buzzi, O.; Bésuelle, P.; Collin, F. Hydro-mechanical modelling of multiphase flow in naturally fractured coalbed using a multiscale approach. *J. Nat. Gas Sci. Eng.* **2020**, *78*, No. 103303.
(45) Jackson, S. J.; Lin, Q.; Krevor, S. Representative elementary volumes, hysteresis, and heterogeneity in multiphase flow from the pore to continuum scale. *Water Resour. Res.* **2020**, *56* (6), No. e2019WR026396.
(46) Barenblatt, G. I.; Zheltov, I. P.; Kochina, I. N. Basic concepts in the theory of seepage of homogeneous liquids in fissured rocks [strata]. *J. Appl. Math. Mech.* **1960**, *24* (5), 1286−1303.
(47) Warren, J. E.; Root, P. J. The behavior of naturally fractured reservoirs. *Soc. Pet. Eng. J.* **1963**, *3* (03), 245−255.
(48) Aguilar-López, J. P.; Bogaard, T.; Gerke, H. H. Dual-permeability model improvements for representation of preferential flow in fractured clays. *Water Resour. Res.* **2020**, *56* (8), No. e2020WR027304.
(49) Shi, R.; Liu, J.; Wang, X.; Wei, M.; Elsworth, D. A critical analysis of shale laboratory permeability evolution data. *Energy* **2021**, *236*, No. 121405.
(50) Wang, Y.; Liu, S. Estimation of pressure-dependent diffusive permeability of coal using methane diffusion coefficient: laboratory measurements and modeling. *Energy Fuels* **2016**, *30* (11), 8968−8976.
(51) Danesh, N. N.; Chen, Z.; Connell, L. D.; Kizil, M. S.; Pan, Z.; Aminossadati, S. M. Characterisation of creep in coal and its impact on permeability: an experimental study. *Int. J. Coal Geol.* **2017**, *173*, 200−211.
(52) Liu, Y.; Zhu, Y.; Chen, S.; Wang, Y.; Song, Y. Evaluation of spatial alignment of kerogen in shale using high-resolution transmission electron microscopy, Raman spectroscopy, and Fourier transform infrared. *Energy Fuels* **2018**, *32* (10), 10616−10627.
(53) Zhang, Q.; Su, Y.; Wang, W.; Lu, M.; Sheng, G. Gas transport behaviors in shale nanopores based on multiple mechanisms and macroscale modeling. *Int. J. Heat Mass Transfer* **2018**, *125*, 845−857.
(54) Patzek, T. W.; Male, F.; Marder, M. Gas production in the Barnett Shale obeys a simple scaling theory. *Proc. Natl. Acad. Sci. U.S.A.* **2013**, *110* (49), 19731−19736.
(55) Patzek, T.; Male, F.; Marder, M. A simple model of gas production from hydrofractured horizontal wells in shales. *AAPG Bull.* **2014**, *98* (12), 2507−2529.
(56) Bear, J. *Dynamics of Fluids in Porous Media*; Courier Corporation, 1988.
(57) Cao, P.; Liu, J.; Leong, Y. K. Combined impact of flow regimes and effective stress on the evolution of shale apparent permeability. *J. Unconv. Oil Gas Resour.* **2016**, *14*, 32−43.
(58) Zhu, W.; Liu, L.; Liu, J.; Wei, C.; Peng, Y. Impact of gas adsorption-induced coal damage on the evolution of coal permeability. *Int. J. Rock Mech. Min. Sci.* **2018**, *101*, 89−97.
(59) Kong, P.; Jiang, L.; Shu, J.; Sainoki, A.; Wang, Q. Effect of fracture heterogeneity on rock mass stability in a highly heterogeneous underground roadway. *Rock Mech. Rock Eng.* **2019**, *52* (11), 4547−4564.
(60) Pan, Z.; Connell, L. D. Modelling permeability for coal reservoirs: a review of analytical models and testing data. *Int. J. Coal Geol.* **2012**, *92*, 1−44.
(61) Cheng, A. H. D. *Poroelasticity*; Springer International Publishing: Switzerland, 2016; Vol. *27*.
(62) Jiang, C.; Zhao, Z.; Zhang, X.; Liu, J.; Elsworth, D.; Cui, G. Controlling effects of differential swelling index on evolution of coal permeability. *J. Rock Mech. Geotech. Eng.* **2020**, *12* (3), 461−472.
(63) Javadpour, F.; Singh, H.; Rabbani, A.; Babaei, M.; Enayati, S. Gas flow models of shale: a review. *Energy Fuels* **2021**, *35* (4), 2999−3010.
(64) Xiong, J.; Liu, X.; Liang, L.; Zeng, Q. Adsorption of methane in organic-rich shale nanopores: An experimental and molecular simulation study. *Fuel* **2017**, *200*, 299−315.
(65) Chen, L.; Zuo, L.; Jiang, Z.; Jiang, S.; Liu, K.; Tan, J.; Zhang, L. Mechanisms of shale gas adsorption: Evidence from thermodynamics and kinetics study of methane adsorption on shale. *Chem. Eng. J.* **2019**, *361*, 559−570.
(66) Cai, J.; Lin, D.; Singh, H.; Wei, W.; Zhou, S. Shale gas transport model in 3D fractal porous media with variable pore sizes. *Mar. Pet. Geol.* **2018**, *98*, 437−447.
(67) Beskok, A.; Karniadakis, G. E. Report: a model for flows in channels, pipes, and ducts at micro and nano scales. *Microscale Thermophys. Eng.* **1999**, *3* (1), 43−77.
(68) Li, W.; Liu, J.; Zeng, J.; Leong, Y. K.; Elsworth, D.; Tian, J.; Li, L. A fully coupled multidomain and multiphysics model for evaluation of shale gas extraction. *Fuel* **2020**, *278*, No. 118214.
(69) Gao, Q.; Han, S.; Cheng, Y.; Li, Y.; Yan, C.; Han, Z. Apparent permeability model for gas transport through micropores and microfractures in shale reservoirs. *Fuel* **2021**, *285*, No. 119086.
(70) Civan, F.; Rai, C. S.; Sondergeld, C. H. Shale-gas permeability and diffusivity inferred by improved formulation of relevant retention and transport mechanisms. *Transp. Porous Media* **2011**, *86* (3), 925−944.
(71) Gandossi, L.; Von Estorff, U.*An Overview of Hydraulic Fracturing and Other Formation Stimulation Technologies for Shale Gas Production*, European Commission JRC Technical Reports201326347 DOI: 10.2790/99937.
(72) Cao, P.; Liu, J.; Leong, Y. K. General gas permeability model for porous media: bridging the gaps between conventional and unconventional natural gas reservoirs. *Energy Fuels* **2016**, *30* (7), 5492−5505.
(73) Zhou, J.; Tian, S.; Zhou, L.; Xian, X.; Yang, K.; Jiang, Y.; Zhang, C.; Guo, Y. Experimental investigation on the influence of sub-and

super-critical CO2 saturation time on the permeability of fractured shale. *Energy* **2020**, *191*, No. 116574.

https://doi.org/10.1021/acs.energyfuels.3c03774
Energy Fuels 2024, 38, 1083−1097